

Theoretical description of a photonic topological insulator based on a cubic lattice of bianisotropic resonators

Alina D. Rozenblit^{1,*} and Nikita A. Olekhno¹

¹*School of Physics and Engineering, ITMO University, 197101 Saint Petersburg, Russia*

(Dated: February 13, 2026)

In the present paper, we construct a theoretical description of a three-dimensional photonic topological insulator in the form of a simple cubic lattice of bianisotropic resonators that is based on a dyadic Green's function approach. By considering electric and magnetic dipole modes and the interactions between different numbers of the nearest resonators, we obtain the Bloch Hamiltonians and the corresponding tight-binding models and analyze the band diagrams, spatial structure of the eigenmodes, and their localization, revealing quadratic degeneracies in the vicinity of high-symmetry points in the absence of bianisotropy and the emergence of in-gap states localized at a domain wall upon the introduction of bianisotropy. Finally, we visualize the Berry curvature distributions to study the topological properties of the considered models.

I. INTRODUCTION

Photonic topological insulators (PTIs) [1, 2] provide a universal framework for the localization of electromagnetic fields at frequencies within the photonic band gap [3]. In addition to frequency separation from the bulk excitations, such states gain additional robustness against various imperfections in the PTI structure due to symmetry protection [4]. While one-dimensional (1D) structures [4, 5] and two-dimensional (2D) metasurfaces [6, 7] appear more compact and thus more suitable for fabrication and applications [8, 9], three-dimensional (3D) PTIs demonstrate a rich hierarchy of surface, hinge, and corner states [10], providing great opportunities to study novel physics such as axion insulators [11, 12] and implement light guiding over complex trajectories [12].

There are various strategies for opening a topological band gap that range from dimerized [13] or shrink-expanded [14] models that preserve time reversal symmetry to the incorporation of magnetic field in the model, either directly via magneto-optical effects [15] or effectively by time modulation [16]. Depending on the considered mechanisms of symmetry breaking that remove spectral degeneracies and result in the opening of a band gap, such PTIs can represent, for example, analogs of Chern insulators (demonstrating quantum Hall effect) with chiral edge states and broken time-reversal symmetry [17], time-reversal analogs to quantum spin Hall [18, 19] or valley Hall [20, 21] insulators with the propagation direction of edge states defined by the pseudospin or valley degrees of freedom, or higher-order topological insulators [10, 22–25].

Recently, the introduction of a bianisotropic response at the level of a single resonator was shown to result in a topological band gap in 1D chains of such resonators [26], as well as 2D [7, 27] and 3D [28, 29] arrays of evenly spaced resonators arranged in simple lattices. Physically, the bianisotropic response achieved via

the breaking of the spatial inversion symmetry of the resonators results in the mixing of electric and magnetic modes that is analogous to the spin-orbit interaction [18]. Hexagonal-lattice based 2D [27, 30] and 3D [28, 29, 31] resonator arrays that demonstrate linear degeneracies in high-symmetry points of the Brillouin zone in the absence of bianisotropy and can be described by effective Dirac Hamiltonians are well-studied theoretically and have been implemented experimentally. However, their square-lattice based counterparts with C_4 rotational symmetry and quadratic degeneracies [32] remain less explored. In particular, 2D square lattice arrays have recently been implemented [7, 33], while a 3D simple cubic lattice has been analyzed within the perturbation theory framework [34], which allows describing the band structure only in the vicinity of high-symmetry points. In addition, bianisotropic resonator arrays can be homogenized and represented as an effective bianisotropic medium [35, 36], although such a description may not fully account for the symmetry of the lattice.

In the present paper, we apply the dyadic Green's function approach [7, 26] to further advance these results and develop a theoretical description of a simple cubic lattice of bianisotropic resonators that allows one to calculate the band structure in the entire Brillouin zone, evaluate Berry curvature, and visualize the eigenmodes in finite arrays. To study the effects of long-range couplings, we consider three different approximations that include the couplings between the nearest, the next-nearest, and the next-to-next nearest resonators. With the help of the obtained model, we analyze the effects of the bianisotropic response magnitude on the band structures and topological properties of the considered 3D PTIs.

The paper is organized as follows. In Section II, we derive Bloch Hamiltonians and real-space tight-binding models for a cubic lattice of bianisotropic resonators using dyadic Green's functions. In Section III, we analyze band diagrams and the density of states. In Section IV, we study the localization properties and spatial profiles of eigenstates in the finite model. Section V is devoted to the topological properties of the proposed models. Fi-

* alina.rozenblit@metalab.ifmo.ru

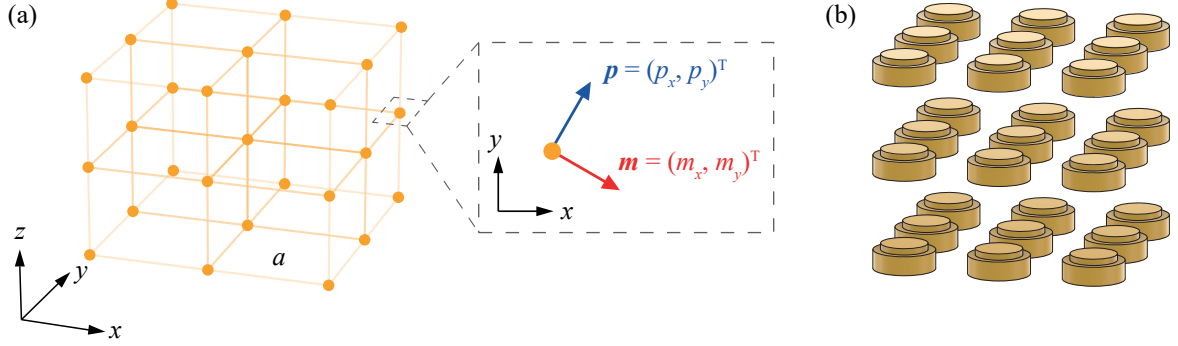


Figure 1. (a) The schematic of point electric and magnetic dipoles arranged in a cubic lattice with period a . The inset points the orientation of the dipoles \mathbf{p} and \mathbf{m} . (b) The example of the model realization as an array of dielectric resonators with inversion symmetry broken shape.

nally, Section VI contains a discussion of the results.

II. THEORETICAL FRAMEWORK

A. Effective Bloch Hamiltonian

In this Section, we extend the coupled-dipole method previously applied to describe a one-dimensional chain [26] and a square lattice [7] of dielectric resonators with a bianisotropic response. We assume that each of the particles in the PTI supports hybridization of the electric and magnetic dipole moments oriented in the xy -plane, while the electromagnetic z -component can be neglected [7]. Thus, we consider point electric $\mathbf{p} = (p_x, p_y)^T$ and magnetic $\mathbf{m} = (m_x, m_y)^T$ dipoles oriented in the xy -plane and arranged in a cubic lattice with period a , as shown in Fig. 1. The components of the excited electric $\mathbf{E} = (E_x, E_y)^T$ and magnetic $\mathbf{H} = (H_x, H_y)^T$ fields and induced dipole moments in a lattice node with coordinates (ia, ja, ka) are related by the polarizability tensor $\hat{\alpha}$

$$\begin{pmatrix} \mathbf{p}^{ijk} \\ \mathbf{m}^{ijk} \end{pmatrix} = \hat{\alpha} \begin{pmatrix} \mathbf{E}^{ijk} \\ \mathbf{H}^{ijk} \end{pmatrix} = \begin{pmatrix} \hat{\alpha}^{ee} & \hat{\alpha}^{em} \\ \hat{\alpha}^{me} & \hat{\alpha}^{mm} \end{pmatrix} \begin{pmatrix} \mathbf{E}^{ijk} \\ \mathbf{H}^{ijk} \end{pmatrix}. \quad (1)$$

which includes the electric $\hat{\alpha}^{ee}$, magnetic $\hat{\alpha}^{mm}$, electromagnetic $\hat{\alpha}^{em}$, and magnetoelectric $\hat{\alpha}^{me}$ components.

We apply the following approximations. First, we consider the case with the electromagnetic duality ($\hat{\varepsilon} = \hat{\mu}$) satisfied, resulting in equal electric and magnetic polarizabilities β along the x - and y -axes $\hat{\alpha}^{ee} = \hat{\alpha}^{mm} = \beta \cdot \hat{\sigma}_0$, where $\hat{\sigma}_0 = (1, 0, 0, 1)$ is the unity matrix. At the same time, reciprocal bianisotropic particles demonstrate the presence of non-vanishing electromagnetic (magnetoelectric) components described by the electromagnetic

coupling χ [37] $\hat{\alpha}^{em} = -\{\hat{\alpha}^{me}\}^T = -\chi \cdot \hat{\sigma}_2$, where $\hat{\sigma}_2 = (0, -i, i, 0)$ is the Pauli matrix. Second, we assume that the diagonal elements of $\hat{\alpha}^{-1}$ depend on the resonance frequency f_0 as $\beta/(\beta^2 - \chi^2) \propto f - f_0$, while the term $\chi/(\beta^2 - \chi^2)$ can be approximated as a constant [38]. Finally, we consider the quasi-static approximation ($k_0 r \ll 1$) of the dyadic Green's function [39], where $r = a((i-m)^2 + (j-n)^2 + (k-l)^2)^{1/2}$ is the distance between the lattice nodes with coordinates (ma, na, la) and (ia, ja, ka) , and k_0 is the wave number. Within such an approximation, only the near-field terms proportional to $1/r^3$ remain.

In order to study the effects of long-range interactions that may sufficiently contribute to the properties of photonic topological insulators [25, 40], we consider three cases: the model with interactions only between the nearest sites separated by the distance $r = a$ (Model I) the model which includes the couplings between the nearest ($r = a$) and the next-nearest ($r = \sqrt{2}a$) sites (Model II), as well as the model which takes into account the interactions between the sites in the first ($r = a$), the second ($r = \sqrt{2}a$), and the third ($r = \sqrt{3}a$) coordination spheres (Model III). Then, applying Bloch's theorem, we obtain the eigenvalue problem $\hat{H}|\psi\rangle = \lambda|\psi\rangle$ in the pseudospin basis $|\psi\rangle = (p_x + m_x, p_y + m_y, p_x - m_x, p_y - m_y)^T$ [28] with eigenvalues $\lambda = a^3 \beta / (\beta^2 - \chi^2)$ and the bianisotropic parameter $\Omega = a^3 \chi / (\beta^2 - \chi^2)$. The full Bloch Hamiltonian \hat{H} has the block-diagonal form

$$\hat{H} = \begin{pmatrix} \hat{H}^\uparrow & 0 \\ 0 & \hat{H}^\downarrow \end{pmatrix}, \quad (2)$$

where $\hat{H}^{\uparrow(\downarrow)}$ are Bloch Hamiltonians for two pseudospins denoted as \uparrow (\downarrow), respectively.

For the three considered approximations in dimensionless units $a = 1$,

$$\hat{H}_I^{\uparrow(\downarrow)} = (\cos k_x + \cos k_y - 2 \cos k_z) \hat{\sigma}_0 + 3(\cos k_x - \cos k_y) \hat{\sigma}_3 \pm \Omega \hat{\sigma}_2 \quad (3)$$

for Model I,

$$\begin{aligned}\hat{H}_{\text{II}}^{\uparrow(\downarrow)} = & \left(\cos k_x + \cos k_y - 2 \cos k_z + \frac{2 \cos k_x \cos k_y - \cos k_x \cos k_z - \cos k_y \cos k_z}{2\sqrt{2}} \right) \hat{\sigma}_0 + \\ & + 3 \left(\cos k_x - \cos k_y + \frac{\cos k_x \cos k_z - \cos k_y \cos k_z}{2\sqrt{2}} \right) \hat{\sigma}_3 - \frac{3}{\sqrt{2}} \sin k_x \sin k_y \hat{\sigma}_1 \pm \Omega \hat{\sigma}_2 \quad (4)\end{aligned}$$

for Model II, and

$$\begin{aligned}\hat{H}_{\text{III}}^{\uparrow(\downarrow)} = & \left(\cos k_x + \cos k_y - 2 \cos k_z + \frac{2 \cos k_x \cos k_y - \cos k_x \cos k_z - \cos k_y \cos k_z}{2\sqrt{2}} \right) \hat{\sigma}_0 + \\ & + 3 \left(\cos k_x - \cos k_y + \frac{\cos k_x \cos k_z - \cos k_y \cos k_z}{2\sqrt{2}} \right) \hat{\sigma}_3 - \left(\frac{3}{\sqrt{2}} + \frac{8}{3\sqrt{3}} \cos k_z \right) \sin k_x \sin k_y \hat{\sigma}_1 \pm \Omega \hat{\sigma}_2 \quad (5)\end{aligned}$$

for Model III, where $\hat{\sigma}_0 = (1, 0, 0, 1)$ is the unity matrix and $\hat{\sigma}_1 = (0, 1, 1, 0)$, $\hat{\sigma}_2 = (0, -i, i, 0)$, and $\hat{\sigma}_3 = (1, 0, 0, -1)$ are the Pauli matrices.

The eigenvalues of pseudospin Hamiltonians are doubly-degenerate for the two values of pseudospin and have the following form for Eq. (3):

$$\begin{aligned}\lambda_{\text{I}}^{\uparrow(\downarrow)} = & \cos k_x + \cos k_y - 2 \cos k_z \pm \left(\Omega^2 + \frac{9}{2} (2 + \right. \\ & \left. + \cos(2k_x) + \cos(2k_y) - 4 \cos k_x \cos k_y) \right)^{1/2}. \quad (6)\end{aligned}$$

The detailed derivation of Bloch Hamiltonians, as well as analytical expressions for the energy bands of pseudospin Hamiltonians Eq. (4) and Eq. (5) are included in Supplemental Material [41].

B. Real-space tight-binding models

To study the spatial structure of eigenmodes in a finite lattice, we consider the real-space tight-binding model described by the following matrix [38] (in units of $a = 1$):

$$\hat{B} = \hat{M} \otimes \hat{G}(r) - \hat{\Omega} \otimes \hat{\sigma}_1 \otimes \hat{\sigma}_2, \quad (7)$$

where \hat{M} is the $[N \times N]$ connectivity matrix describing the connections between lattice sites with $N = N_x N_y N_z$ being the total number of sites in a cubic lattice: the matrix element $M_{st} = 1$ if the sites labeled by indices s and t with coordinates (x_s, y_s, z_s) and (x_t, y_t, z_t) are connected with a link, $M_{st} = 0$ otherwise, and the diagonal elements $M_{tt} = 0$, and $\hat{G}(r)$ is the dyadic Green's function in the near-field approximation that depends on the distance $r = r_{st} = ((x_s - x_t)^2 + (y_s - y_t)^2 + (z_s - z_t)^2)^{1/2}$ between the sites s and t . Thus, the first term on the right hand side of Eq. (7) defines the interactions between the electric (magnetic) dipoles in different sites. The second term describes the hybridization of the electric and magnetic dipole moments in each of the lattice sites that is governed by the $[N \times N]$ bianisotropy parameter matrix $\Omega_{st} = \Omega(x_s, y_s, z_s) \delta_{st}$, where $\Omega(x_s, y_s, z_s)$ is the value of bianisotropy parameter in a certain site s

with coordinates (x_s, y_s, z_s) . We consider the following coordinate dependence of the bianisotropy parameter in a lattice with $N_x \times 2N_y \times N_z$ sites:

$$\Omega(x, y, z) = \Omega(y) = \begin{cases} \Omega & , y < N_y \\ -\Omega & , y \geq N_y \end{cases}. \quad (8)$$

This configuration corresponds to a domain wall between two cubic sublattices formed by $N_x \times N_y \times N_z$ resonators with opposite signs of the bianisotropy parameter for the domains.

III. SPECTRAL PROPERTIES

The obtained pseudospin Bloch Hamiltonians $\hat{H}^{\uparrow(\downarrow)}$ each have two eigenvalue bands, whereas the eigenvalues of the full Bloch Hamiltonians \hat{H} that correspond to the opposite pseudospins come in doubly-degenerate Kramers pairs [42]. Figures 2(a)–2(c) show the band diagrams in the Brillouin zone in the absence of bianisotropy ($\Omega = 0$) for each of the considered Models I, II, and III, respectively. The eigenvalues are plotted along the $\Gamma(0, 0, 0) - X(\pi, 0, 0) - M(\pi, \pi, 0) - \Gamma(0, 0, 0) - Z(0, 0, \pi) - R(\pi, 0, \pi) - A(\pi, \pi, \pi) - Z(0, 0, \pi)$ trajectory, with additional insets showing the dispersion between X - R and M - A high-symmetry points.

It is seen that in the absence of bianisotropy, the bands for Model I host fourfold-degenerate nodal lines between the points M - Γ , Γ - Z , A - Z , and M - A , Fig. 2(a). However, once the interactions between the next-nearest sites are taken into account, the degeneracies between high-symmetry points M - Γ and A - Z are lifted, as demonstrated in Fig. 2(b). Additional couplings between the lattice sites in the third coordination sphere only slightly change the dispersion between the diagonally-opposite high-symmetry points M - Γ and A - Z , Fig. 2(c). Importantly, quadratic fourfold degeneracies are observed at high-symmetry points Γ , M , Z , and A in all the considered models, in contrast to the linear Dirac-like de-

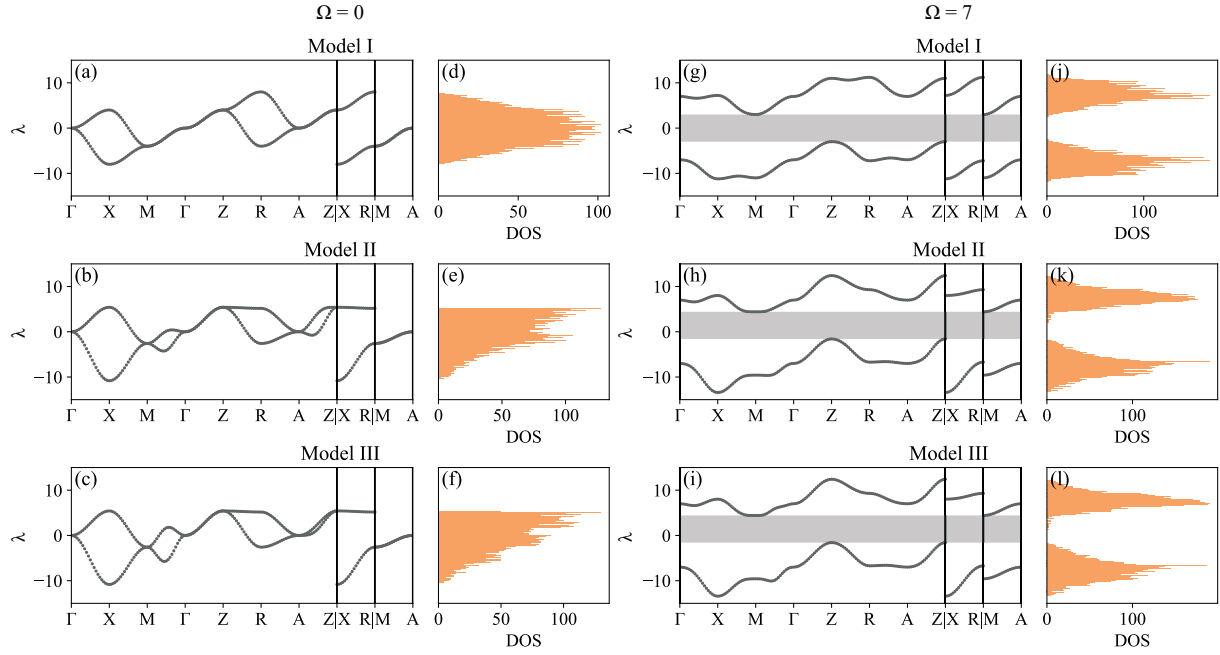


Figure 2. (a)-(c) Energy bands of the Bloch Hamiltonians for (a) Model I (the nearest neighbors), Eq. (3); (b) Model II (the next-nearest neighbors), Eq. (4); and (c) Model III (the next-to-next nearest neighbors), Eq. (5) in the absence of bianisotropy ($\Omega = 0$). (d)-(f) Density of states $\rho(\lambda)$ for tight-binding models corresponding to cubic lattices of $10 \times 20 \times 10$ sites without bianisotropy ($\Omega = 0$) for (d) Model I, (e) Model II, and (f) Model III real-space Hamiltonians plotted as histogram with 150 bins. Panels (g)-(l) are the same as (a)-(f), but for non-zero bianisotropic parameter $\Omega = 7$. The gray shaded areas in dispersion diagrams (g)-(i) highlight the bandgaps.

generacies characteristic of 3D resonator arrays based on stacked hexagonal lattices [28] or their 2D counterparts [27], in analogy to a 2D square lattice of bianisotropic resonators [7]. Finally, Models II and III feature well-pronounced flat bands between the points $Z-R$ and $X-R$ for the upper energy band, Figs. 2(b) and 2(c).

Along with band diagrams for Bloch Hamiltonians, we also numerically evaluate the eigenvalues for finite-size tight-binding lattices from Eq. (7). Then, we consider the density of states (DOS)

$$\rho(\lambda) = \sum_j \delta(\lambda - \lambda_j), \quad (9)$$

where the index j enumerates all eigenvalues λ_j and $\delta(\lambda - \lambda_j)$ is the pseudo-delta function defined in the following way: $\delta(\lambda - \lambda_j) = 0$ for $\lambda \neq \lambda_j$ and $\delta(\lambda - \lambda_j) = 1$ for $\lambda = \lambda_j$. Numerically, the DOS can be obtained by plotting a histogram of the evaluated eigenvalues. In Figs. 2(d)-2(f), the density of states $\rho(\lambda)$ is shown for the lattices with $10 \times 20 \times 10$ sites. It is seen in Fig. 2(d) that for Model I with interactions between only the nearest sites taken into account, the DOS is symmetric with respect to $\lambda = 0$, despite the absence of chiral symmetry in the model that requires a complete symmetry of the band structure with respect to $\lambda = 0$. In turn, the introduction of additional couplings between the next-nearest (Model II) and the next-to-next nearest (Model III) sites breaks this DOS symmetry, as shown in Figs. 2(e) and 2(f).

Moreover, the DOS $\rho(\lambda)$ for Models II and III in Figs. 2(e) and 2(f) features the presence of pronounced peaks at the upper bands that are also a hallmark of flat bands. Indeed, flat bands correspond to the vanishing group velocity $\partial\lambda/\partial k$ and therefore to a singularity in the density of states $\rho(\lambda) \propto \partial k/\partial\lambda$ for $\lambda \approx 5$.

Upon the introduction of bianisotropy, all three models feature the emergence of band gaps, as shown in Figs. 2(g)-2(i) for $\Omega = 7$. As discussed in the Supplemental Material [41], the width of the band gaps is linearly proportional to Ω . In this case, all degeneracies are lifted, except for two-fold Kramers degeneracy. Moreover, the band structures for Models II and III become more similar compared to the case without bianisotropy, as seen in Figs. 2(h) and 2(i). The formation of band gaps is also observed in the DOS shown in Figs. 2(j)-2(l). While Model I demonstrates the symmetry in DOS for non-zero values of the bianisotropic parameter, as shown in Fig. 2(j), the DOS for Models II and III remain asymmetric with respect to $\lambda = 0$; see Figs. 2(k) and 2(l). In contrast to the case with $\Omega = 0$, there are no flat bands in the upper energy band for Models II and III, as seen both from band diagrams and from the DOS. However, a nearly-flat band region is observed in the lower energy bands between the points $R-A$ in Figs. 2(h) and 2(i), with corresponding peaks in the DOS, Figs. 2(k) and 2(l). Finally, Models II and III feature the emergence of in-gap eigenstates in DOS seen in Figs. 2(k) and 2(l).

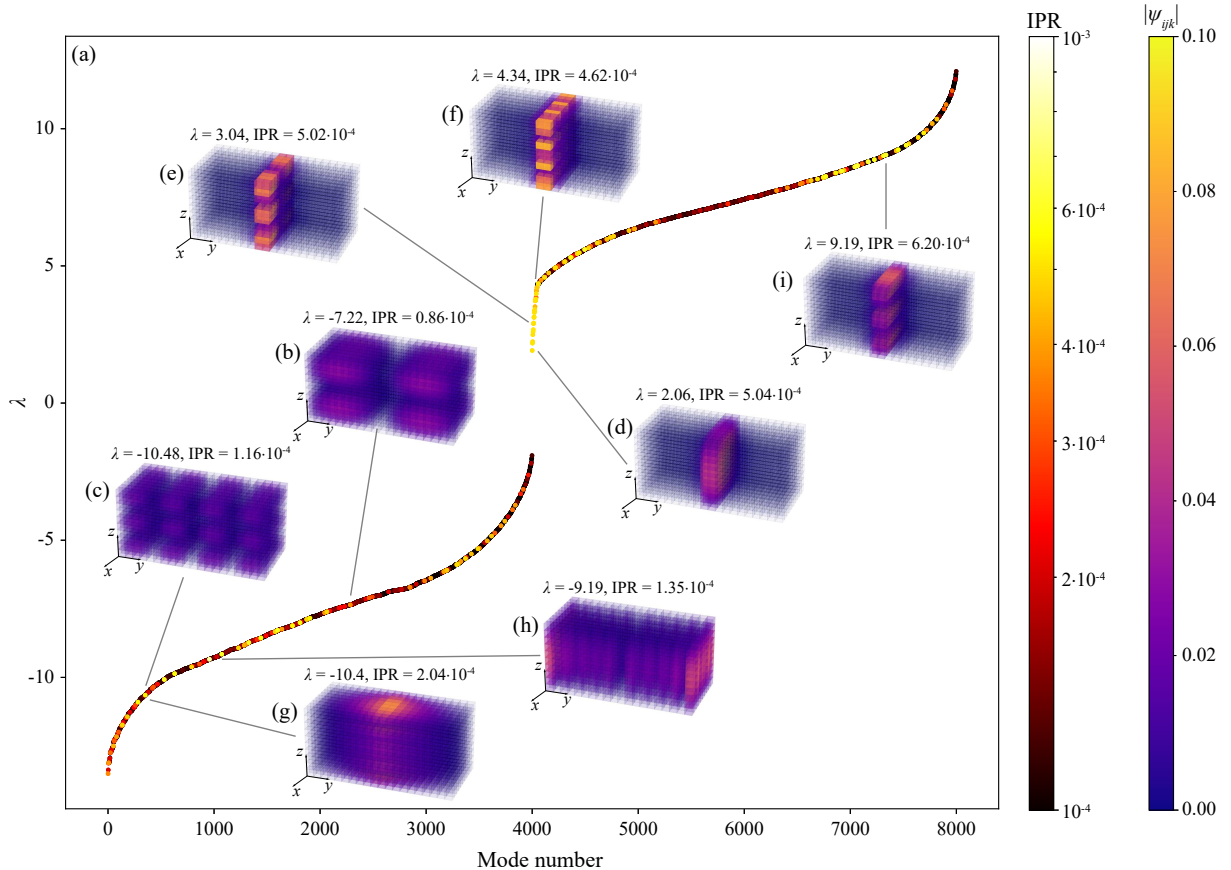


Figure 3. (a) Spectrum of eigenvalues λ for the system consisting of two domains with $10 \times 10 \times 10$ sites and bianisotropic parameters $\Omega = 7$ and $\Omega = -7$, respectively. Color shows the inverse participation ratio Eq. (10). (b)-(i) Eigenfunctions profiles corresponding to the absolute value of pseudospin-up polarization $p_x + m_x$ shown by color, which demonstrate (b),(c) bulk states, (d)-(f) interface states localized at the domain wall in the bandgap, (g) an interface state hybridized with a bulk mode, (h) a bulk mode with dominant surface localization at the boundary, and (i) an edge state in the continuum.

IV. LOCALIZATION AND SPATIAL PROFILES OF EIGENSTATES

Next, we consider the spatial distributions of the eigenmodes and analyze their localization by evaluating the inverse participation ratios (IPR) [43]:

$$\text{IPR}(\lambda) = \sum_{i,j,k} |\psi_{ijk}(\lambda)|^4, \quad (10)$$

where $|\psi_{ijk}(\lambda)| = (\sum_{\alpha=1}^4 |\psi_{ijk}^{\alpha}(\lambda)|^2)^{1/2}$ is the amplitude of the eigenmode corresponding to the eigenvalue λ at the site with coordinates (i, j, k) normalized by the condition $\sum_{i,j,k} |\psi_{ijk}|^2 = 1$, and the index α denotes four on-site scalar components in the considered pseudospin basis $p_x + m_x$, $p_y + m_y$, $p_x - m_x$, and $p_y - m_y$. The summation is performed over all sites (i, j, k) in a finite tight-binding model. Such a definition allows us to characterize the localization of eigenstates simultaneously for all pseudospin components, in order to exclude the possible situation when a certain component is localized while some other one is not. For strongly delocalized states,

IPR Eq. (10) takes low values of the order of $1/N$, where N is the total number of sites, while for localized states it tends to unity (in the limiting case when the eigenmode is completely localized at one site).

Figure 3(a) shows a numerically calculated spectrum of the tight-binding model corresponding to Model II and consisting of two domains with bianisotropic parameters $\Omega = 7$ and $\Omega = -7$, each having the size $10 \times 10 \times 10$ sites. Thus, the resulting tight-binding model includes $10 \times 20 \times 10$ sites and features a domain wall in its middle. The points corresponding to the energy values in Fig. 3(a) are colored according to their IPR. It is seen that the bulk bands mostly include delocalized states that have the form of standing waves with different numbers of wave nodes in the x -, y -, and z -directions, as shown in Fig. 3(b) and 3(c). The states in the band gap are strongly localized at the domain wall, as seen in Fig. 3(d), 3(e), and 3(f). Such interface states also have different numbers of nodes in the y - and z -directions, with higher energy states having more nodes starting from zero in the lowest energy state in Fig. 3(d). Thus, the in-gap states seen in the DOS in Fig. 2 represent interface states, whose

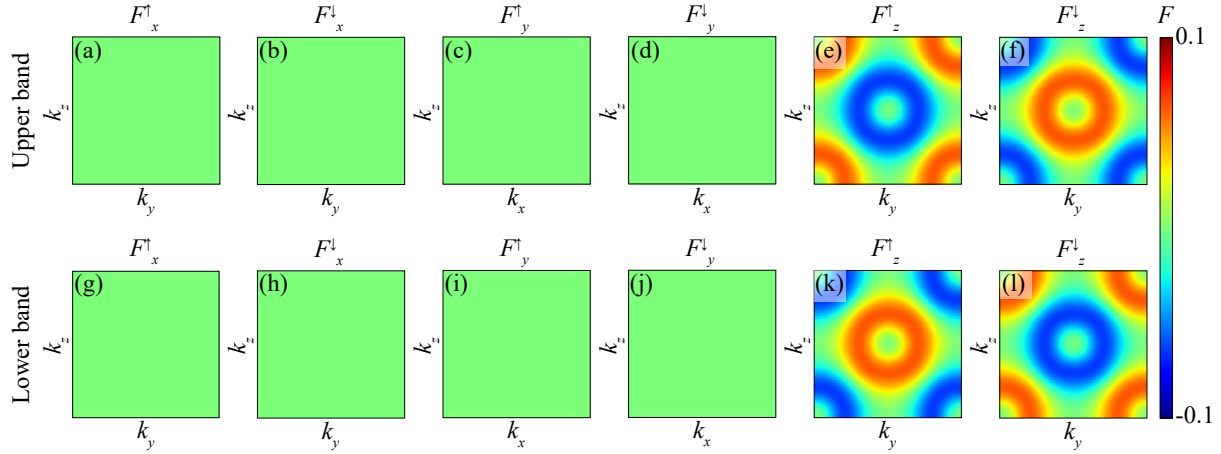


Figure 4. Numerically evaluated Berry curvature distributions for two pseudospins for the (a)-(f) upper and (g)-(l) lower energy bands of the Hamiltonian Eq. (4) with bianisotropic parameter $\Omega = 7$.

topological properties will be analyzed further.

Along with delocalized states similar to Fig. 3(b) and 3(c), the bulk bands demonstrate the presence of eigenmodes with higher localization, e.g., Fig. 3(g), 3(h), and 3(i). For example, there are eigenmodes in the form of hybridized interface states and bulk excitations, Fig. 3(g), and bulk modes with pronounced localization at the outer surfaces of domains; see Fig. 3(h). Finally, there are states localized at the domain wall with energies in the continuum that feature high IPR values, as demonstrated in Fig. 3(i). However, in contrast to in-gap states, such modes may hybridize with bulk excitations in a realistic system with losses taken into account, making their experimental implementation unrealistic.

V. BERRY CURVATURE

To study the topological properties of the considered models, we visualize the distributions of Berry curvature $F_{\xi}^{\uparrow(\downarrow)}$ calculated from the normalized Bloch Hamiltonian eigenvectors $\psi(k)$ for three orthogonal planes of the cubic lattice using the following expression [44]:

$$F_{\xi}^{\uparrow(\downarrow)}(k_{\zeta}, k_{\eta}, k_{\xi} = 0) = \frac{\partial}{\partial k_{\zeta}} \langle \psi_{1(2)}^{\uparrow(\downarrow)} | \frac{\partial}{\partial k_{\eta}} | \psi_{1(2)}^{\uparrow(\downarrow)} \rangle - \frac{\partial}{\partial k_{\eta}} \langle \psi_{1(2)}^{\uparrow(\downarrow)} | \frac{\partial}{\partial k_{\zeta}} | \psi_{1(2)}^{\uparrow(\downarrow)} \rangle, \quad (11)$$

where the indices $\zeta \neq \eta \neq \xi$ take the values $\{x, y, z\}$, the subscript 1(2) denotes the upper or lower eigenvalue band of the pseudospin Hamiltonians, and the superscript $\uparrow(\downarrow)$ corresponds to the pseudospin-up or pseudospin-down Hamiltonians $\hat{H}^{\uparrow(\downarrow)}$, respectively.

We proceed with the calculation of Berry curvatures for the Hamiltonians corresponding to each of the considered approximations. In the absence of bianisotropy

($\Omega = 0$), each of the eigenvalue bands in the considered models features vanishing Berry curvatures $F_x^{\uparrow(\downarrow)}$, $F_y^{\uparrow(\downarrow)}$, and $F_z^{\uparrow(\downarrow)}$ in the Brillouin zone, pointing to the trivial topology [45]. This follows from the simultaneous presence of time-reversal symmetry and spatial inversion symmetries along all three axes [46].

Upon the introduction of non-zero bianisotropic parameter $\Omega = 7$, Model I still exhibits zero Berry curvature for all three planes, see Supplemental Materials [41]. However, Models II and III demonstrate the emergence of non-zero F_z distribution in the xy -plane, as shown in Fig. 4 considering Model II as an example. In particular, two regions are observed around M and Γ high symmetry points with opposite signs of the Berry curvature F_z . Since F_x and F_y zero out even in the presence of bianisotropic coupling, the considered cubic resonator array represents a weak PTI formed by the stacking of 2D square lattice layers [7] along the z direction, in analogy to a 3D structure of stacked hexagonal layers [29]. It is seen that Berry curvature distributions change sign for different band indices and opposite pseudospins. The results obtained for Model I agree with the absence of in-gap eigenstates in DOS seen in Fig. 2(j) and demonstrate that in order to describe the topological properties of such lattices of bianisotropic resonators, it is necessary to take into account the interactions between the resonators within at least the second coordination sphere.

VI. DISCUSSION

In the present paper, we considered theoretically a simple cubic lattice of bianisotropic resonators applying the dyadic Green's function approach [7, 26] to extend the results of effective description based on perturbation theory [34] and address the localization properties of the eigenmodes as well as topological properties of the model.

It is shown that the introduction of a bianisotropic response leads to the opening of the band gap, similarly to the 2D hexagonal [27] and square [7] resonator lattices, as well as 3D PTIs formed by stacking hexagonal layers [28].

In order to study the effects of long-range couplings that are known to be crucial for the description of a band gap formation in two-dimensional square lattices [40] or can even give rise to additional types of corner states in photonic HOTI [25], we compared the band structures of three model Hamiltonians taking into account the couplings between the nearest, next-nearest, and next-to-next nearest sites. It is shown that a pronounced change in the band structure is observed when the next-nearest couplings are added, while the couplings in the third coordination sphere slightly modify the dispersion diagram. Moreover, the nearest-neighbor approximation is shown to result in additional degeneracies and leads to trivial Berry curvature distributions even in the photonic insulating phase for a non-zero bianisotropy parameter. Thus, it is necessary to take into account at least the next-nearest couplings in order to properly describe the properties of cubic lattices of bianisotropic resonators. The considered models demonstrate 2D interface states and are shown to be weak PTIs by the evaluation of Berry curvature.

For further development of the considered model, it looks perspective to consider the following directions. First, the model considers only electric and magnetic dipoles in the (xy) plane. Taking into account dipoles along the z -axis will allow one to consider a more general case of resonator shape when the approximations valid for the previous experimental realizations [7, 27, 29] are

not satisfied. Moreover, including a quadrupole near-field response [47] or taking into account higher multipoles [48] can also result in interesting physics. Second, we consider the case where the resonator size, the lattice constant, and the size of the structure are subwavelength, and thus only near-field contributions are taken into account. However, there are examples of PTIs that demonstrate an interplay of near- and long-range couplings [49] or consider far-field properties of resonator arrays [6, 29]. Thus, it appears interesting to consider intermediate-field and far-field contributions in dyadic Green's functions as well, which may increase the complexity of the model but can result in a set of interesting effects. Finally, the model can be extended to more complex unit cells, e.g., by including dimerization or staggering [5, 50] to realize a hierarchy of lower-dimensional hinge or corner states, or by considering nonlinear effects [51].

For experimental realization of the considered model at microwave frequencies, ceramic cylindrical resonators can be applied, in analogy to 2D hexagonal [27] and square [7] lattices, as well as a recent demonstration of a 3D array of stacked hexagonal layers [29]. Moreover, metallic resonators implemented as printed circuit boards can also be applied [33]. From a practical perspective, such resonator arrays can be applied to control field localization or implement signal routing along complex trajectories by designing specific shapes of the domain interfaces.

ACKNOWLEDGMENTS

We acknowledge fruitful discussions with Dmitry Zhirihin and Georgy Kurganov. The work is supported by the Russian Science Foundation (project 24-79-10314).

[1] Ling Lu, John D Joannopoulos, and Marin Soljačić, “Topological photonics,” *Nature Photonics* **8**, 821–829 (2014).

[2] Tomoki Ozawa, Hannah M. Price, Alberto Amo, Nathan Goldman, Mohammad Hafezi, Ling Lu, Mikael C. Rechtsman, David Schuster, Jonathan Simon, Oded Zilberman, and Iacopo Carusotto, “Topological photonics,” *Reviews of Modern Physics* **91**, 015006 (2019).

[3] Daniel Leykam, Haoran Xue, Baile Zhang, and Y. D. Chong, “Limitations and possibilities of topological photonics,” *Nature Reviews Physics* **8**, 55–64 (2026).

[4] Sergey Kruk, Alexander Poddubny, Daria Smirnova, Lei Wang, Alexey Slobozhanyuk, Alexander Shorokhov, Ivan Kravchenko, Barry Luther-Davies, and Yuri Kivshar, “Nonlinear light generation in topological nanostructures,” *Nature Nanotechnology* **14**, 126–130 (2019).

[5] Daniel A Bobylev, Daria A Smirnova, and Maxim A Gorlach, “Photonic topological states mediated by staggered bianisotropy,” *Laser & Photonics Reviews* **15**, 1900392 (2021).

[6] Maxim A Gorlach, Xiang Ni, Daria A Smirnova, Dmitry Korobkin, Dmitry Zhirihin, Alexey P Slobozhanyuk, Pavel A Belov, Andrea Alù, and Alexander B Khanikaev, “Far-field probing of leaky topological states in all-dielectric metasurfaces,” *Nature Communications* **9**, 909 (2018).

[7] Alina D Rozenblit, Georgiy D Kurganov, Dmitry V Zhirihin, and Nikita A Olekhno, “Topological edge states in all-dielectric square-lattice arrays of bianisotropic microwave resonators,” *Physical Review B* **111**, 085415 (2025).

[8] Shukai Ma and Steven M Anlage, “Microwave applications of photonic topological insulators,” *Applied Physics Letters* **116** (2020), <https://doi.org/10.1063/5.0008046>.

[9] Viktor M. Puchnin, Olga V. Matvievskaya, Alexey P. Slobozhanyuk, Alena V. Shchelokova, and Nikita A. Olekhno, “Application of topological edge states in magnetic resonance imaging,” *Physical Review Applied* **20**, 024076 (2023).

[10] Ziyao Wang, Yan Meng, Bei Yan, Dong Zhao, Linyun Yang, Jingming Chen, Minqi Cheng, Tao Xiao, Perry Ping Shum, Gui-Geng Liu, Yihao Yang, Hongsheng Chen, Xiang Xi, Zhen-Xiao Zhu, Biye Xie, and Zhen Gao, “Realization of a three-dimensional photonic

higher-order topological insulator,” *Nature Communications* **16**, 3122 (2025).

[11] Gui-Geng Liu, Subhaskar Mandal, Xiang Xi, Qiang Wang, Chiara Devescovi, Antonio Morales-Pérez, Ziyao Wang, Linyun Yang, Rimi Banerjee, Yang Long, Yan Meng, Peiheng Zhou, Zhen Gao, Yidong Chong, Aitzol García-Etxarri, Maia G. Vergniory, and Baile Zhang, “Photonic axion insulator,” *Science* **387**, 162–166 (2025).

[12] Hua-Shan Lai, Yan-Chen Zhou, Ze-Qun Sun, Cheng He, and Yan-Feng Chen, “Photonic axion insulator with non-coplanar chiral hinge transport,” *Nature Communications* **16**, 3826 (2025).

[13] W. P. Su, J. R. Schrieffer, and A. J. Heeger, “Solitons in polyacetylene,” *Physical Review Letters* **42**, 1698–1701 (1979).

[14] Long-Hua Wu and Xiao Hu, “Scheme for achieving a topological photonic crystal by using dielectric material,” *Physical Review Letters* **114**, 223901 (2015).

[15] Zheng Wang, Yidong Chong, John D Joannopoulos, and Marin Soljačić, “Observation of unidirectional backscattering-immune topological electromagnetic states,” *Nature* **461**, 772–775 (2009).

[16] Kejie Fang, Zongfu Yu, and Shanhui Fan, “Realizing effective magnetic field for photons by controlling the phase of dynamic modulation,” *Nature Photonics* **6**, 782–787 (2012).

[17] F. D. M. Haldane and S. Raghu, “Possible realization of directional optical waveguides in photonic crystals with broken time-reversal symmetry,” *Physical Review Letters* **100**, 013904 (2008).

[18] Alexander B Khanikaev, S Hossein Mousavi, Wang-Kong Tse, Mehdi Kargarian, Allan H MacDonald, and Gennady Shvets, “Photonic topological insulators,” *Nature Materials* **12**, 233–239 (2013).

[19] Biye Xie, Guangxu Su, Hong-Fei Wang, Feng Liu, Lumang Hu, Si-Yuan Yu, Peng Zhan, Ming-Hui Lu, Zhenlin Wang, and Yan-Feng Chen, “Higher-order quantum spin Hall effect in a photonic crystal,” *Nature Communications* **11**, 3768 (2020).

[20] Jiho Noh, Sheng Huang, Kevin P. Chen, and Mikael C. Rechtsman, “Observation of photonic topological valley hall edge states,” *Physical Review Letters* **120**, 063902 (2018).

[21] Fei Gao, Haoran Xue, Zhaoju Yang, Kueifu Lai, Yang Yu, Xiao Lin, Yidong Chong, Gennady Shvets, and Baile Zhang, “Topologically protected refraction of robust kink states in valley photonic crystals,” *Nature Physics* **14**, 140–144 (2018).

[22] Wladimir A. Benalcazar, B. Andrei Bernevig, and Taylor L. Hughes, “Quantized electric multipole insulators,” *Science* **357**, 61–66 (2017).

[23] Bi-Ye Xie, Guang-Xu Su, Hong-Fei Wang, Hai Su, Xiao-Peng Shen, Peng Zhan, Ming-Hui Lu, Zhen-Lin Wang, and Yan-Feng Chen, “Visualization of higher-order topological insulating phases in two-dimensional dielectric photonic crystals,” *Physical Review Letters* **122**, 233903 (2019).

[24] Xiao-Dong Chen, Wei-Min Deng, Fu-Long Shi, Fu-Li Zhao, Min Chen, and Jian-Wen Dong, “Direct observation of corner states in second-order topological photonic crystal slabs,” *Physical Review Letters* **122**, 233902 (2019).

[25] Mengyao Li, Dmitry Zhirihin, Maxim Gorlach, Xiang Ni, Dmitry Filonov, Alexey Slobozhanyuk, Andrea Alù, and Alexander B Khanikaev, “Higher-order topological states in photonic kagome crystals with long-range interactions,” *Nature Photonics* **14**, 89–94 (2020).

[26] Alexey A Gorlach, Dmitry V Zhirihin, Alexey P Slobozhanyuk, Alexander B Khanikaev, and Maxim A Gorlach, “Photonic Jackiw-Rebbi states in all-dielectric structures controlled by bianisotropy,” *Physical Review B* **99**, 205122 (2019).

[27] Alexey Slobozhanyuk, Alena V. Shchelokova, Xiang Ni, S. Hossein Mousavi, Daria A. Smirnova, Pavel A. Belov, Andrea Alù, Yuri S. Kivshar, and Alexander B. Khanikaev, “Near-field imaging of spin-locked edge states in all-dielectric topological metasurfaces,” *Applied Physics Letters* **114**, 031103 (2019).

[28] Alexey Slobozhanyuk, S Hossein Mousavi, Xiang Ni, Daria Smirnova, Yuri S Kivshar, and Alexander B Khanikaev, “Three-dimensional all-dielectric photonic topological insulator,” *Nature Photonics* **11**, 130–136 (2017).

[29] Dmitry V. Zhirihin, Mikhail S. Sidorenko, Alina D. Rozenblit, Georgiy D. Kurganov, Maxim A. Gorlach, Dmitry S. Filonov, Yuri S. Kivshar, and Alexey P. Slobozhanyuk, “Helical metasurfaces based on topological surface states in three-dimensional photonic topological insulators,” *Nature Materials* (2026), 10.1038/s41563-026-02488-8.

[30] Xiaojun Cheng, Camille Jouvaud, Xiang Ni, S Hossein Mousavi, Azriel Z Genack, and Alexander B Khanikaev, “Robust reconfigurable electromagnetic pathways within a photonic topological insulator,” *Nature Materials* **15**, 542–548 (2016).

[31] Yihao Yang, Zhen Gao, Haoran Xue, Li Zhang, Mengjia He, Zhaoju Yang, Ranjan Singh, Yidong Chong, Baile Zhang, and Hongsheng Chen, “Realization of a three-dimensional photonic topological insulator,” *Nature* **565**, 622–626 (2019).

[32] Y. D. Chong, Xiao-Gang Wen, and Marin Soljačić, “Effective theory of quadratic degeneracies,” *Physical Review B* **77**, 235125 (2008).

[33] Alexey P Slobozhanyuk, Alexander B Khanikaev, Dmitry S Filonov, Daria A Smirnova, Andrey E Miroshnichenko, and Yuri S Kivshar, “Experimental demonstration of topological effects in bianisotropic metamaterials,” *Scientific Reports* **6**, 22270 (2016).

[34] Tetsuyuki Ochiai, “Gapless surface states originating from accidentally degenerate quadratic band touching in a three-dimensional tetragonal photonic crystal,” *Physical Review A* **96**, 043842 (2017).

[35] Qinghua Guo, Oubo You, Biao Yang, James B Sellman, Edward Blythe, Hongchao Liu, Yuanjiang Xiang, Jensen Li, Dianyuan Fan, Jing Chen, *et al.*, “Observation of three-dimensional photonic dirac points and spin-polarized surface arcs,” *Physical Review Letters* **122**, 203903 (2019).

[36] Ruey-Lin Chern, Yang-Jie Shen, and You-Zhong Yu, “Photonic topological insulators in bianisotropic metamaterials,” *Optics Express* **30**, 9944–9958 (2022).

[37] Viktar S Asadchy, Ana Díaz-Rubio, and Sergei A Tretyakov, “Bianisotropic metasurfaces: physics and applications,” *Nanophotonics* **7**, 1069–1094 (2018).

[38] Minkyung Kim and Junsuk Rho, “CDPDS: coupled dipole method-based photonic dispersion solver,” *Computer Physics Communications* **282**, 108493 (2023).

[39] Chen-To Tai, *Dyadic Green Functions in Electromagnetic*

Theory, 2nd ed. (IEEE Press, 1994).

[40] Nikita A Olekhno, Alina D Rozenblit, Valerii I Kachin, Alexey A Dmitriev, Oleg I Burnistrov, Pavel S Seregin, Dmitry V Zhirikhin, and Maxim A Gorlach, “Experimental realization of topological corner states in long-range-coupled electrical circuits,” *Physical Review B* **105**, L081107 (2022).

[41] See Supplemental Material at [URL] for (i) the detailed derivation of Bloch Hamiltonians in different approximations; (ii) analytical expressions for energy bands in the considered models and the study of their dependence on the bianisotropic parameter; and (iii) a comparison of Berry curvature distributions for the considered models.,

[42] Liang Fu and Charles L Kane, “Topological insulators with inversion symmetry,” *Physical Review B* **76**, 045302 (2007).

[43] David J. Thouless, “Electrons in disordered systems and the theory of localization,” *Physics Reports* **13**, 93–142 (1974).

[44] F. D. M. Haldane, “Berry curvature on the Fermi surface: Anomalous Hall effect as a topological Fermi-liquid property,” *Physical Review Letters* **93**, 206602 (2004).

[45] Minkyung Kim, Zubin Jacob, and Junsuk Rho, “Recent advances in 2D, 3D and higher-order topological photonics,” *Light: Science & Applications* **9**, 130 (2020).

[46] Di Xiao, Ming-Che Chang, and Qian Niu, “Berry phase effects on electronic properties,” *Reviews of Modern Physics* **82**, 1959–2007 (2010).

[47] Raymond PH Wu and HC Ong, “Small mode volume topological photonic states in one-dimensional lattices with dipole-quadrupole interactions,” *Physical Review Research* **4**, 023233 (2022).

[48] Maxim Mazanov, Anton S. Kupriianov, Roman S. Savelev, Zuxian He, and Maxim A. Gorlach, “Multipole higher-order topology in a multimode lattice,” *Physical Review B* **109**, L201122 (2024).

[49] Caifu Fan, Xi Shi, Feng Wu, Yunhui Li, Haitao Jiang, Yong Sun, and Hong Chen, “Photonic topological transition in dimerized chains with the joint modulation of near-field and far-field couplings,” *Photonics Research* **10**, 41–49 (2022).

[50] Xiaoting Sang, Junpeng Hou, Yazhou Gu, Ya-Jie Wu, and Zhitong Li, “All-dielectric photonic higher-order topological insulator induced by a staggered bianisotropy,” *Physical Review A* **109**, 063518 (2024).

[51] Daria Smirnova, Daniel Leykam, Yidong Chong, and Yuri Kivshar, “Nonlinear topological photonics,” *Applied Physics Reviews* **7**, 021306 (2020).

Supplemental Material

Theoretical description of a photonic topological insulator based on a cubic lattice of bianisotropic resonators

Alina D. Rozenblit^{1,*} and Nikita A. Olekhno¹

¹*School of Physics and Engineering, ITMO University, 197101 Saint Petersburg, Russia*

(Dated: February 13, 2026)

CONTENTS

S1. Bloch Hamiltonian	1
S2. Band dispersion	4
S3. Berry curvature for different approximations	5
References	6

S1. BLOCH HAMILTONIAN

In this Section, we provide a detailed derivation of the Bloch Hamiltonian. We consider a cubic lattice with period a formed by point electric $\mathbf{p} = (p_x, p_y)^T$ and magnetic $\mathbf{m} = (m_x, m_y)^T$ dipoles oriented in the xy -plane, as shown in Fig. 1(a) in the main text. The components of the excited electric $\mathbf{E} = (E_x, E_y)^T$ and magnetic $\mathbf{H} = (H_x, H_y)^T$ fields and induced dipole moments in a lattice site with coordinates (ia, ja, ka) are related by the polarizability tensor $\hat{\alpha}$ as

$$\begin{pmatrix} \mathbf{p}^{ijk} \\ \mathbf{m}^{ijk} \end{pmatrix} = \hat{\alpha} \begin{pmatrix} \mathbf{E}^{ijk} \\ \mathbf{H}^{ijk} \end{pmatrix}. \quad (1)$$

In turn, the polarizability tensor includes the electric $\hat{\alpha}^{ee}$, magnetic $\hat{\alpha}^{mm}$, electromagnetic $\hat{\alpha}^{em}$, and magnetoelectric $\hat{\alpha}^{me}$ components:

$$\hat{\alpha} = \begin{pmatrix} \hat{\alpha}^{ee} & \hat{\alpha}^{em} \\ \hat{\alpha}^{me} & \hat{\alpha}^{mm} \end{pmatrix}. \quad (2)$$

Next, we consider the case with the electromagnetic duality ($\hat{\epsilon} = \hat{\mu}$) satisfied, resulting in equal electric and magnetic polarizabilities β along the x - and y -axes, which yields

$$\hat{\alpha}^{ee} = \hat{\alpha}^{mm} = \beta \cdot \hat{\sigma}_0, \quad (3)$$

where $\hat{\sigma}_0 = (1, 0; 0, 1)$ is the unity matrix. At the same time, reciprocal bianisotropic particles demonstrate the presence of non-vanishing electromagnetic (magnetoelectric) components described by the electromagnetic coupling χ [1]:

$$\hat{\alpha}^{em} = -\{\hat{\alpha}^{me}\}^T = -\chi \cdot \hat{\sigma}_2, \quad (4)$$

where $\hat{\sigma}_2 = (0, -i; i, 0)$ is the Pauli matrix. Thus, the polarizability tensor takes the following form:

$$\hat{\alpha} = \begin{pmatrix} \beta & 0 & 0 & i\chi \\ 0 & \beta & -i\chi & 0 \\ 0 & i\chi & \beta & 0 \\ -i\chi & 0 & 0 & \beta \end{pmatrix}. \quad (5)$$

* alina.rozenblit@metalab.ifmo.ru

The electromagnetic field components can be expressed through dipole moments with the help of the inverse polarizability tensor $\widehat{\alpha}^{-1}$:

$$\begin{pmatrix} \mathbf{E}^{ijk} \\ \mathbf{H}^{ijk} \end{pmatrix} = \widehat{\alpha}^{-1} \begin{pmatrix} \mathbf{p}^{ijk} \\ \mathbf{m}^{ijk} \end{pmatrix}, \quad (6)$$

where

$$\widehat{\alpha}^{-1} = \frac{1}{\beta^2 - \chi^2} \begin{pmatrix} \beta & 0 & 0 & -i\chi \\ 0 & \beta & i\chi & 0 \\ 0 & -i\chi & \beta & 0 \\ i\chi & 0 & 0 & \beta \end{pmatrix}. \quad (7)$$

For simplicity, we assume that the diagonal elements of $\widehat{\alpha}^{-1}$ depend on the resonance frequency f_0 as $\beta/(\beta^2 - \chi^2) \propto f - f_0$, while the term $\chi/(\beta^2 - \chi^2)$ can be approximated as a constant [2]. Converting $\widehat{\alpha}^{-1}$ to dimensionless values and taking into account the approximations, we obtain eigenvalues $\lambda = a^3\beta/(\beta^2 - \chi^2)$ and the bianisotropic parameter $\Omega = a^3\chi/(\beta^2 - \chi^2)$. Thus, (6) can be rewritten in the following form:

$$\begin{pmatrix} \mathbf{E}^{ijk} \\ \mathbf{H}^{ijk} \end{pmatrix} = \left(\frac{\lambda}{a^3} \widehat{\sigma}_0 \otimes \widehat{\sigma}_0 + \frac{\Omega}{a^3} \widehat{\sigma}_1 \otimes \widehat{\sigma}_2 \right) \begin{pmatrix} \mathbf{p}^{ijk} \\ \mathbf{m}^{ijk} \end{pmatrix}, \quad (8)$$

where $\widehat{\sigma}_1 = (0, 1; 1, 0)$ is the Pauli matrix.

On the other hand, the electromagnetic field amplitudes at a certain site can be found as the sum of fields excited by dipoles from other sites and expressed via dyadic Green functions:

$$\begin{pmatrix} \mathbf{E}^{ijk} \\ \mathbf{H}^{ijk} \end{pmatrix} = \sum_{\substack{m \neq i \\ n \neq j \\ l \neq k}} \begin{pmatrix} \widehat{G}^{ee}(r, k_0) & \widehat{G}^{em}(r, k_0) \\ \widehat{G}^{me}(r, k_0) & \widehat{G}^{mm}(r, k_0) \end{pmatrix} \begin{pmatrix} \mathbf{p}^{mnl} \\ \mathbf{m}^{mnl} \end{pmatrix}. \quad (9)$$

where $r = a\sqrt{(i-m)^2 + (j-n)^2 + (k-l)^2}$ is the distance between the lattice sites with coordinates (ma, na, la) and (ia, ja, ka) , and k_0 is the wave number. The bianisotropic parts of the dyadic Green function are related as $\widehat{G}^{em} = -\widehat{G}^{me}$, while the electromagnetic duality requires $\widehat{G}^{ee} = \widehat{G}^{mm}$. Dyadic Green functions can be calculated using the following equations [3]:

$$G_{\zeta\eta}^{ee} = (\partial_\zeta \partial_\eta + k_0^2 \delta_{\zeta\eta}) \frac{e^{ik_0 r_{ij}}}{r_{ij}}, \quad (10)$$

$$G_{\zeta\eta}^{em} = ik_0 \varepsilon_{\zeta\eta\kappa} \partial_\kappa \frac{e^{ik_0 r_{ij}}}{r_{ij}}, \quad (11)$$

where $\delta_{\zeta\eta}$ stands for the Kronecker delta, $\varepsilon_{\zeta\eta\kappa}$ is the Levi-Civita symbol, and $\partial_\zeta = \partial/\partial\zeta$. The parameters ζ, η, κ take the values $\{x, y, z\}$. Considering the spacing between the dipoles as a function of the distance along the x -, y -, and z -axes $r = \sqrt{x^2 + y^2 + z^2}$, we obtain the following expressions for the dyadic Green function components:

$$\begin{aligned} G_{xx}^{ee} &= \frac{e^{ik_0 r}}{r^3} \left(\frac{x^2}{r^2} (3 - 3ik_0 r - k_0^2 r^2) + ik_0 r + k_0^2 r^2 - 1 \right), \\ G_{yy}^{ee} &= \frac{e^{ik_0 r}}{r^3} \left(\frac{y^2}{r^2} (3 - 3ik_0 r - k_0^2 r^2) + ik_0 r + k_0^2 r^2 - 1 \right), \\ G_{xy}^{ee} &= G_{yx}^{ee} = \frac{e^{ik_0 r}}{r^3} \left(\frac{xy}{r^2} (3 - 3ik_0 r - k_0^2 r^2) \right), \\ G_{xx}^{em} &= -G_{yy}^{em} = 0, \\ G_{xy}^{em} &= -G_{yx}^{em} = \frac{e^{ik_0 r}}{r^3} (-ik_0 r - k_0^2 r^2). \end{aligned} \quad (12)$$

In the following, we focus on the near-field approximation ($k_0 r \ll 1$) of the dyadic Green function, in which only the near-field terms proportional to $1/r^3$ remain, and rewrite the distances between the sites in (12) through their

coordinates:

$$\begin{aligned} G_{xx}^{\text{ee}} &= \frac{3a^2(m-i)^2}{r^5} - \frac{1}{r^3}, \\ G_{yy}^{\text{ee}} &= \frac{3a^2(n-j)^2}{r^5} - \frac{1}{r^3}, \\ G_{xy}^{\text{ee}} = G_{yx}^{\text{ee}} &= \frac{3a^2(m-i)(n-j)}{r^5}, \\ G_{xx}^{\text{em}} = G_{yy}^{\text{em}} = G_{xy}^{\text{em}} = G_{yx}^{\text{em}} &= 0. \end{aligned} \quad (13)$$

As the first model, we consider the cubic lattice with interactions only between the nearest sites ($r = a$). In this case, (9) has the following form:

$$\begin{pmatrix} \mathbf{E}^{ijk} \\ \mathbf{H}^{ijk} \end{pmatrix} = \sum_{\substack{m=i \pm 1 \\ n=j \\ l=k}} \begin{pmatrix} \hat{G}^{\text{ee}} & \hat{G}^{\text{em}} \\ \hat{G}^{\text{me}} & \hat{G}^{\text{mm}} \end{pmatrix} \begin{pmatrix} \mathbf{p}^{mnl} \\ \mathbf{m}^{mnl} \end{pmatrix} + \sum_{\substack{m=i \\ n=j \pm 1 \\ l=k}} \begin{pmatrix} \hat{G}^{\text{ee}} & \hat{G}^{\text{em}} \\ \hat{G}^{\text{me}} & \hat{G}^{\text{mm}} \end{pmatrix} \begin{pmatrix} \mathbf{p}^{mnl} \\ \mathbf{m}^{mnl} \end{pmatrix} + \sum_{\substack{m=i \\ n=j \\ l=k \pm 1}} \begin{pmatrix} \hat{G}^{\text{ee}} & \hat{G}^{\text{em}} \\ \hat{G}^{\text{me}} & \hat{G}^{\text{mm}} \end{pmatrix} \begin{pmatrix} \mathbf{p}^{mnl} \\ \mathbf{m}^{mnl} \end{pmatrix}. \quad (14)$$

Applying Bloch's theorem results in (14) taking the following form:

$$\begin{pmatrix} \mathbf{E}^{ijk} \\ \mathbf{H}^{ijk} \end{pmatrix} = a^{-3} \left((\cos k_x a + \cos k_y a - 2 \cos k_z a) \hat{\sigma}_0 \otimes \hat{\sigma}_0 + 3(\cos k_x a - \cos k_y a) \hat{\sigma}_0 \otimes \hat{\sigma}_3 \right) \begin{pmatrix} \mathbf{p}^{ijk} \\ \mathbf{m}^{ijk} \end{pmatrix}. \quad (15)$$

Finally, we compare the right hand sides of (8) and (15), consider dimensionless units $a = 1$, and rewrite the result in the form of an eigenvalue problem $\hat{H}'_I |\psi'\rangle = \lambda |\psi'\rangle$. Thus, the effective Bloch Hamiltonian in the basis $|\psi'\rangle = (p_x, p_y, m_x, m_y)^T$ in the nearest-neighbor approximation (denoted by the lower index I) is given by the following expression:

$$\hat{H}'_I = (\cos k_x + \cos k_y - 2 \cos k_z) \hat{\sigma}_0 \otimes \hat{\sigma}_0 + 3(\cos k_x - \cos k_y) \hat{\sigma}_0 \otimes \hat{\sigma}_3 - \Omega \hat{\sigma}_1 \otimes \hat{\sigma}_2. \quad (16)$$

To convert the obtained Bloch Hamiltonian \hat{H}'_I to a block-diagonal form, the basis $|\psi'\rangle$ should be replaced by the pseudospin basis $|\psi\rangle = (p_x + m_x, p_y + m_y, p_x - m_x, p_y - m_y)^T$ [4]. Thus, we apply the following unitary transformation matrix \hat{U} :

$$\hat{U} = \frac{1}{\sqrt{2}} \begin{pmatrix} 1 & 0 & 1 & 0 \\ 0 & 1 & 0 & 1 \\ 1 & 0 & -1 & 0 \\ 0 & 1 & 0 & -1 \end{pmatrix}, \quad (17)$$

and evaluate $\hat{H}_I = \hat{U} \hat{H}'_I \hat{U}^\dagger$. Finally, the full Bloch Hamiltonian \hat{H} in the pseudospin basis has the form

$$\hat{H} = \begin{pmatrix} \hat{H}^\uparrow & 0 \\ 0 & \hat{H}^\downarrow \end{pmatrix}, \quad (18)$$

where $\hat{H}^{\uparrow(\downarrow)}$ are Bloch Hamiltonians for two pseudospins denoted as $\uparrow(\downarrow)$, respectively. Within the nearest neighbor approximation (Model I), these pseudospin Hamiltonians are given by

$$\hat{H}_I^{\uparrow(\downarrow)} = (\cos k_x + \cos k_y - 2 \cos k_z) \hat{\sigma}_0 + 3(\cos k_x - \cos k_y) \hat{\sigma}_3 \pm \Omega \hat{\sigma}_2. \quad (19)$$

Next, we consider the model that includes the couplings between the nearest ($r = a$) and the next-nearest ($r = \sqrt{2}a$) sites (Model II), as well as the model that takes into account the interactions between the sites in the first ($r = a$), the second ($r = \sqrt{2}a$), and the third ($r = \sqrt{3}a$) coordination spheres (Model III) in (14). Then, we obtain the following Bloch Hamiltonians $\hat{H}_{\text{II}}^{\uparrow(\downarrow)}$ and $\hat{H}_{\text{III}}^{\uparrow(\downarrow)}$ in the pseudospin basis $|\psi\rangle = (p_x + m_x, p_y + m_y, p_x - m_x, p_y - m_y)^T$:

$$\begin{aligned} \hat{H}_{\text{II}}^{\uparrow(\downarrow)} &= \left(\cos k_x + \cos k_y - 2 \cos k_z + \frac{2 \cos k_x \cos k_y - \cos k_x \cos k_z - \cos k_y \cos k_z}{2\sqrt{2}} \right) \hat{\sigma}_0 + \\ &+ 3 \left(\cos k_x - \cos k_y + \frac{\cos k_x \cos k_z - \cos k_y \cos k_z}{2\sqrt{2}} \right) \hat{\sigma}_3 - \frac{3}{\sqrt{2}} \sin k_x \sin k_y \hat{\sigma}_1 \pm \Omega \hat{\sigma}_2 \end{aligned} \quad (20)$$

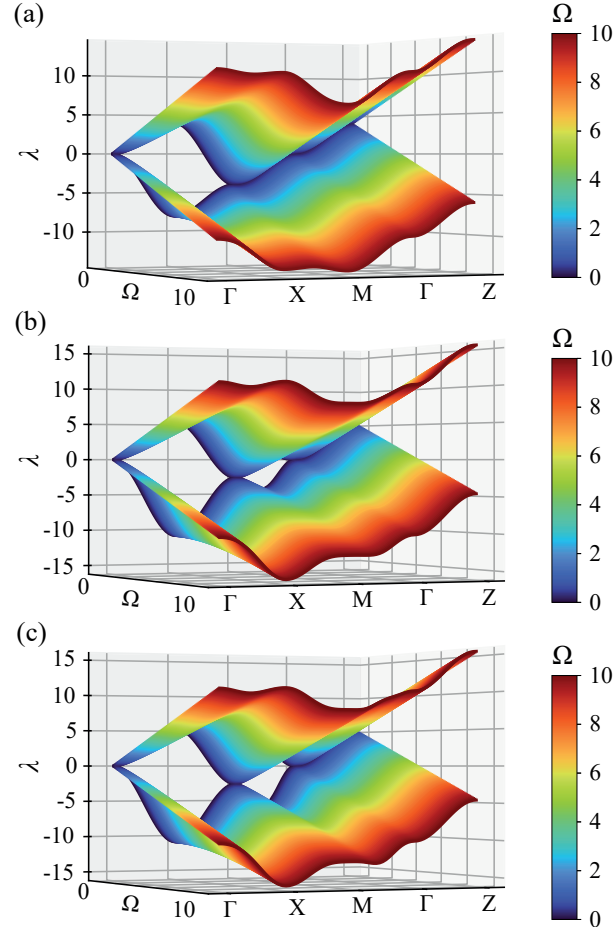


Figure S1. The dispersion diagrams for different values of the bianisotropic parameter Ω along Γ - X - M - Γ - Z trajectory between the high-symmetry points of the Brillouin zone for (a) Model I, (19); (b) Model II, (20); and (c) Model III, (21)

and

$$\begin{aligned} \hat{H}_{\text{III}}^{\uparrow(\downarrow)} = & \left(\cos k_x + \cos k_y - 2 \cos k_z + \frac{2 \cos k_x \cos k_y - \cos k_x \cos k_z - \cos k_y \cos k_z}{2\sqrt{2}} \right) \hat{\sigma}_0 + \\ & + 3 \left(\cos k_x - \cos k_y + \frac{\cos k_x \cos k_z - \cos k_y \cos k_z}{2\sqrt{2}} \right) \hat{\sigma}_3 - \left(\frac{3}{\sqrt{2}} + \frac{8}{3\sqrt{3}} \cos k_z \right) \sin k_x \sin k_y \hat{\sigma}_1 \pm \Omega \hat{\sigma}_2. \quad (21) \end{aligned}$$

S2. BAND DISPERSION

Analytical expressions for the energy bands of pseudospin Hamiltonians (20) and (21) have the following form. For Model I,

$$\lambda_1 = \cos k_x + \cos k_y - 2 \cos k_z \pm 3 \left\{ 1 + \frac{\Omega^2}{9} + \frac{\cos(2k_x) + \cos(2k_y)}{2} - 2 \cos k_x \cos k_y \right\}^{1/2}. \quad (22)$$

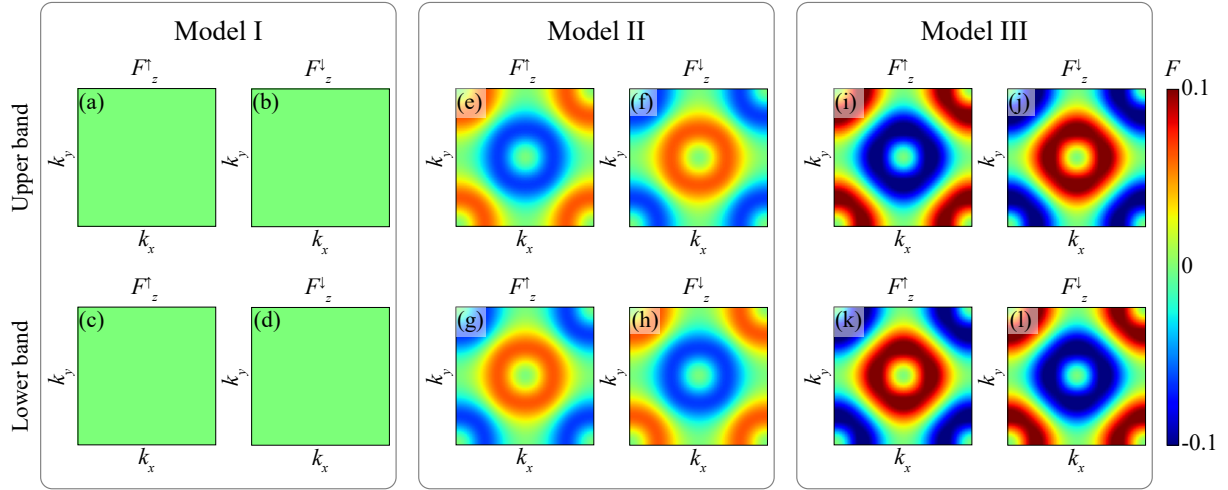


Figure S2. Numerically calculated distributions of the Berry curvature F_z for (a)-(f) Model I, (e)-(h) Model II, and (i)-(l) Model III for the two pseudospins and two energy bands in the case of bianisotropic parameter $\Omega = 7$.

For Model II, the eigenvalues are

$$\begin{aligned} \lambda_{II} = & \cos k_x + \cos k_y - 2 \cos k_z + \frac{1}{2\sqrt{2}} (2 \cos k_x \cos k_y - \cos k_x \cos k_z - \cos k_y \cos k_z) \pm \\ & \pm \frac{1}{8} \left\{ 684 + 64\Omega^2 + 234 \cos(2k_x) - 1224 \cos k_x \cos k_y + 234 \cos(2k_y) + \right. \\ & \left. + 72 \cos(2k_x) \cos(2k_y) + 36 (\cos k_x - \cos k_y)^2 (8\sqrt{2} \cos k_z + \cos(2k_z)) \right\}^{1/2}. \quad (23) \end{aligned}$$

Finally, for Model III,

$$\begin{aligned} \lambda_{III} = & \cos k_x + \cos k_y - 2 \cos k_z + \frac{1}{2\sqrt{2}} (2 \cos k_x \cos k_y - \cos k_x \cos k_z - \cos k_y \cos k_z) \pm \\ & \pm \frac{1}{12\sqrt{6}} \left\{ 9490 + 864\Omega^2 + 2903 \cos(2k_y) - 72\sqrt{2} (-54 - 8\sqrt{3} + (8\sqrt{3} - 27) \cos(2k_y)) \cos k_z + \right. \\ & + (742 - 13 \cos(2k_y)) \cos(2k_z) - 972 \cos k_x \cos k_y (17 + 8\sqrt{2} \cos k_z + \cos(2k_z)) + \\ & + \cos(2k_x) (2903 + 72\sqrt{2} (27 - 8\sqrt{3}) \cos k_z - 13 \cos(2k_z) + \\ & \left. + 4 \cos(2k_y) (307 + 144\sqrt{6} \cos k_z + 64 \cos(2k_z))) \right\}^{1/2}. \quad (24) \end{aligned}$$

As seen from (22)–(24), the eigenvalues are linearly proportional to the value of the bianisotropic parameter $\lambda \propto |\Omega|$, which is observed in Fig. S1.

S3. BERRY CURVATURE FOR DIFFERENT APPROXIMATIONS

In the section, we study the Berry curvatures $F_z(k_x, k_y)$ calculated with the help of Eq. (11) in the main text for each of the considered approximations in the case of a nonzero bianisotropic parameter $\Omega = 7$. The upper and lower bands of the pseudospin-up and pseudospin-down Hamiltonians (19), corresponding to Model I, possess the vanishing Berry curvature $F_z(k_x, k_y)$ for any values of wavenumbers k_x and k_y , as shown in Figs. S2(a)–S2(d). Therefore, a cubic lattice of electric and magnetic dipoles with the nearest-neighbor interactions is topologically trivial even in the presence of bianisotropic response. However, Berry curvature F_z is no longer trivial as soon as the couplings between the next-nearest sites are added to the model, as illustrated in Figs. S2(e)–S2(h). In particular, two regions are observed around Γ and M high-symmetry points with opposite signs of Berry curvature F_z . The change between the bands and pseudospins is accompanied by a change in the sign of Berry curvature. The introduction of the interactions between the lattice sites in the third coordination sphere demonstrates the features of the Berry

curvature distributions similar to those obtained for Model II. The main difference is the increase in non-zero values of the Berry curvature, as depicted in Figs. S2(i)–S2(l). Thus, we have demonstrated that the introduction of the couplings between the next-nearest sites is required to properly describe the topological properties of a cubic lattice of bianisotropic resonators.

[1] Viktor S Asadchy, Ana Díaz-Rubio, and Sergei A Tretyakov, “Bianisotropic metasurfaces: physics and applications,” *Nanophotonics* **7**, 1069–1094 (2018).

[2] Minkyung Kim and Junsuk Rho, “CDPDS: coupled dipole method-based photonic dispersion solver,” *Computer Physics Communications* **282**, 108493 (2023).

[3] Chen-To Tai, *Dyadic Green Functions in Electromagnetic Theory*, 2nd ed. (IEEE Press, 1994).

[4] Alexey Slobozhanyuk, S Hossein Mousavi, Xiang Ni, Daria Smirnova, Yuri S Kivshar, and Alexander B Khanikaev, “Three-dimensional all-dielectric photonic topological insulator,” *Nature Photonics* **11**, 130–136 (2017).